



LAWRENCE  
LIVERMORE  
NATIONAL  
LABORATORY

# DENSITY-FUNCTIONAL STUDY OF BCC U-Mo, Np-Mo, Pu-Mo, AND Am-Mo ALLOYS

A. Landa, P. Soderlind, P. E. A. Turchi

August 30, 2012

Journal of Nuclear Materials

## **Disclaimer**

---

This document was prepared as an account of work sponsored by an agency of the United States government. Neither the United States government nor Lawrence Livermore National Security, LLC, nor any of their employees makes any warranty, expressed or implied, or assumes any legal liability or responsibility for the accuracy, completeness, or usefulness of any information, apparatus, product, or process disclosed, or represents that its use would not infringe privately owned rights. Reference herein to any specific commercial product, process, or service by trade name, trademark, manufacturer, or otherwise does not necessarily constitute or imply its endorsement, recommendation, or favoring by the United States government or Lawrence Livermore National Security, LLC. The views and opinions of authors expressed herein do not necessarily state or reflect those of the United States government or Lawrence Livermore National Security, LLC, and shall not be used for advertising or product endorsement purposes.

# **Density-functional study of bcc U-Mo, Np-Mo, Pu-Mo, and Am-Mo alloys**

**A. Landa<sup>\*</sup>, P. Söderlind, P.E.A. Turchi**

**Lawrence Livermore National Laboratory, Livermore, CA 94551, USA**

## **Abstract**

Density-functional theory, previously used to describe phase equilibria in the  $\gamma$ -U-Mo alloys [A. Landa, P. Söderlind, P.E.A. Turchi, J. Nucl. Mater. 414 (2011) 132], is extended to study ground-state properties of the bcc-based ( $\gamma$ ) X-Mo (X = Np, Pu, Am) solid solutions. We discuss how the heat of formation correlates with the charge transfer between the alloy components, and how magnetism influences the deviation from Vegard's law for the equilibrium atomic volume.

Keywords: nuclear reactor materials, phase transitions, first principles.

---

<sup>\*</sup> Corresponding author. Tel.: +1 925 424 3523; fax: +1 925 422 2851. E-Mail address: [landa1@llnl.gov](mailto:landa1@llnl.gov)

## 1. Introduction

In our previous papers [1, 2] we performed detailed *ab initio* studies of the fundamental thermodynamic properties of the body-centered-cubic (bcc) or  $\gamma$ -phase of the U-Zr and U-Mo systems that are candidates as metallic nuclear fuels for fast breeder reactors. We found that a significantly larger absolute value of the charge transfer from U atoms in the case of the  $\gamma$ -U-Mo alloys than in the case of the  $\gamma$ -U-Zr alloys causes the ponderable negative Madelung energy contribution to the heat of formation of the  $\gamma$ -U-Mo alloys in comparison with one for the  $\gamma$ -U-Zr alloys [2]. This difference in the absolute value of the charge transfer from U atoms results in much higher constituent redistribution in  $\gamma$ -U-Zr than in  $\gamma$ -U-Mo fuels where a single  $\gamma$ -phase field exists and can be retained (quenched) as a metastable phase up to room temperature.

Although U-Zr and U-Mo alloys can be used as nuclear fuels, a fast reactor operation on a closed fuel cycle will, due to nuclear reactions, contain Pu [3, 4] as well as minor actinides (MA), Np, Am, and Cm [5-7]. Semi-empirical model calculations [8], supported by experimental observations, indicate that the excess enthalpy of solution of the  $\gamma$ -U-Zr phase controls the constituent redistribution process. In our previous papers [1, 9-11] we performed detailed calculations of the heat of formation of bcc-based ( $\gamma$ ) X-Zr (X = U, Np, Pu, Am) solid solutions, which can be used for further analysis of the constituent redistribution in the central zone of  $\gamma$ -U-Zr nuclear fuels. We found that theoretical heats of formation of the  $\gamma$ -U-Zr,  $\gamma$ -Np-Zr, and  $\gamma$ -Pu-Zr alloys are in a good agreement with data derived from a CALPHAD assessment [12-14] of the experimental thermodynamics and phase diagram information for these systems, although we could not

perform a similar assessment in the case of the Am-Zr system due to the total lack of experimental thermodynamics data and absence of the phase diagram.

As was mentioned above, we undertook an *ab initio* study of the fundamental thermodynamic properties of  $\gamma$ -U-Mo alloys [2] while thermodynamic properties of U-TRU-Mo alloys have not been modeled yet. Thus, in the present study we report results of *ab initio* calculations for bcc-based ( $\gamma$ ) X-Mo (X = Np, Pu, Am) alloys. We believe that our results are essential because experimental data on these alloys are lacking and theoretical phase diagrams, available for Np-Mo [15], Pu-Mo [16], and Am-Mo [17] alloys, are based on the simple Brewer valence bond model [18] with no input from experimental data. Similar to the Am-Zr system, a lack of experimental thermodynamics data prevents us for performing a CALPHAD comparison for X-Mo (X = Np, Pu, Am) alloys.

For our calculations we employ two complementary computational techniques: (i) the scalar-relativistic (SR) or fully relativistic (FR) exact muffin-tin orbital method (EMTO) and (ii) the full-potential linear muffin-tin orbital method (FPLMTO) that accounts for all relativistic effects. The SR-EMTO method was used in the case of U-Mo and Np-Mo alloys and FR-EMTO method for the Pu-Mo and Am-Mo alloys (previous studies [9, 19] revealed that relativistic effects are important for Pu- and Am-based alloys). Pertinent details of the computational methods are described in Section 2. Results of the density-functional calculations of the ground-state properties of the  $\gamma$ -U-Mo,  $\gamma$ -Np-Mo,  $\gamma$ -Pu-Mo, and  $\gamma$ -Am-Mo solid solutions are presented in Section 3. We provide discussion in Section 4. Lastly, concluding remarks are presented in Section 5.

## 2. Computational details

The calculations we have referred to as EMTO are performed using the Green's-function technique based on the improved screened Korringa-Kohn-Rostoker method, where the one-electron potential is represented by optimized overlapping muffin-tin (OOMT) potential spheres [20, 21]. Inside the potential spheres the potential is spherically symmetric, and it is constant between the spheres. The radius of the potential spheres, the spherical potential inside these spheres, and the constant value in the interstitial region are determined by minimizing (i) the deviation between the exact and overlapping potentials, and (ii) the errors caused by the overlap between the spheres. Within the EMTO formalism, the one-electron states are calculated exactly for the OOMT potentials. As an output of the EMTO calculations, one can determine self-consistent Green's function of the system and the complete, non-spherically symmetric charge density. Finally, the total energy is calculated using the full charge-density technique [22]. We treat, as the valence states, the  $7s$ ,  $6p$ ,  $6d$ , and  $5f$  states for U, Np, Pu, and Am and  $5s$ ,  $4p$ , and  $4d$  states for Mo. The corresponding Kohn-Sham orbitals are expanded in terms of *spdf* exact muffin-tin orbitals, i.e. we adopt an orbital momentum cutoff,  $l_{max} = 3$ . The EMTO orbitals, in turn, consist of the *spdf* partial waves (solutions of the radial Schrödinger equation for the spherical OOMT potential wells) and the *spdf* screened spherical waves (solutions of the Helmholtz equation for the OOMT muffin-tin zero potential). The completeness of the muffin-tin basis was discussed in details in Ref. [21] and it was shown that for metals crystallizing in close-packed lattices  $l_{max} = 3$  (*spdf* orbitals) leads to the well converged charge density and total energy. For the electron exchange and correlation energy functional, the generalized gradient approximation

(GGA) is considered [23]. Integration over the Brillouin zone is performed using the special  $k$ -point technique [24] with 506 points in the irreducible wedge of the zone for the bcc structure. The moments of the density of states, needed for the kinetic energy and valence charge density, are calculated by integrating the Green's function over a complex energy contour (with 2.5-3.0 Ry diameter) using a Gaussian integration technique with 30-40 points on a semi-circle enclosing the occupied states. In the case of the implementation of the FR-EMTO formalism, the spin-orbit coupling is included through the four-component Dirac equation [25].

In order to treat compositional disorder the EMTO method is combined with the coherent potential approximation (CPA) [26, 27]. The ground-state properties of the chemically random bcc-based ( $\gamma$ ) X-Mo (X = U, Np, Pu, Am) alloys are obtained from EMTO-CPA calculations that include the Coulomb screening potential and energy [28-30]. The screening constants are determined from supercell calculations using the locally self-consistent Green's-function (LSGF) method [31] for a 1024 atoms supercell that models the random equiatomic alloys. The  $\alpha$  and  $\beta$  screening constants (see Refs. [28, 29] for details) are found to be 0.725 and 1.088, 0.726 and 1.083, 0.655 and 0.953, and 0.585 and 0.802, for the bcc U-Mo, Np-Mo, Pu-Mo, and Am-Mo alloys, respectively.

The Pu-Mo and Am-Mo alloys have been modeled within the disordered local moment (DLM) approximation that leads to a paramagnetic solution, see Refs. [32, 33] for details. The equilibrium atomic density of these alloys is obtained from a Murnaghan fit to the total energy versus lattice constant curve [34].

For the elemental metals, the most accurate and fully relativistic calculations are performed using a full-potential (no geometrical approximations) approach, where the

relativistic effects, including spin-orbit coupling, are accounted for through the conventional perturbative scheme [35] that has the accuracy of solving the Dirac equation for the light actinides [36]. Although unable to model disorder in the CPA sense it provides important information for the metals, and also serves to confirm the CPA calculations mentioned above. For this purpose we use a version of the FPLMTO [37], in which the “full potential” in FPLMTO refers to the use of non-spherical contributions to the electron charge density and potential. This is accomplished by expanding the charge density and potential in cubic harmonics inside non-overlapping muffin-tin spheres and in a Fourier series in the interstitial region. We use two energy tails associated with each basis orbital, and for the semi-core  $6s$  and  $6p$  states and valence states ( $7s$ ,  $7p$ ,  $6d$ , and  $5f$ ) these pairs are different. With this ‘double basis’ approach we use a total of six energy tail parameters and a total of 12 basis functions per atom. Spherical harmonic expansions are carried out up to  $l_{max}=6$  for the basis, potential, and charge density. As in the case of the EMTO method, GGA is used for the electron exchange-correlation approximation. Finally, a special quasi-random structure (SQS) method, utilizing a 16-atom supercell (different for 25 at. % and 75 at. % concentration versus the 50 at. % concentration) was used to treat the compositional disorder within the FPLMTO formalism [38], so the results could be compared with those obtained with EMTO-CPA. Spin polarization for the Pu- and Am-containing alloys was arranged in an antiferromagnetic fashion [39] with neighboring atoms having anti-parallel spins. This is different from the spin configuration used in the EMTO calculations where the spins are randomly aligned.

The two methods (EMTO-CPA and FPLMTO-SQS) generally produce similar quantitative results although some numerical differences are expected due to their



different electronic-structure implementations. Beyond that, the alloy approximation as well as the magnetic treatment (Pu and Am containing alloys) is different between the two approaches. Because of the many contrasting details it is difficult to relate any discrepancy of the results to particular approximations. It suffices to say that FPLMTO is a more accurate electronic-structure method while CPA is a more robust approximation for the alloy system.

### 3. Ground-state properties of the bcc U-Mo, Np-Mo, Pu-Mo and Am-Mo solid solutions

Fig. 1a shows results of EMTO-CPA calculations of the heat of formation of the  $\gamma$ -U-Mo solid solutions at  $T = 0$  K [2]. The calculated heat of formation is positive in a broad region of the composition interval but changes its sign from positive to negative when uranium composition exceeds  $\sim 80$  at. %. For comparison, we also show the heats of formation for the  $\text{U}_{75}\text{Mo}_{25}$ ,  $\text{U}_{50}\text{Mo}_{50}$ , and  $\text{U}_{25}\text{Mo}_{75}$  bcc alloys [2], calculated within the FPLMTO-SQS technique that agrees relatively well with EMTO-CPA results. This plot also shows CAPHAD assessment [40] of the heat of formation of the  $\gamma$ -U-Mo solid solutions at  $T = 100$  K with a distinctive change of its sign from positive to negative around 80 at. % of uranium.

Fig. 1b shows results of EMTO-CPA and FPLMTO-SQS calculations of the heat of formation of the  $\gamma$ -Np-Mo solid solutions at  $T = 0$  K. In contrast to the  $\gamma$ -U-Mo solid solution, where the heat of formation changes its sign from positive to negative on the U-rich side of the composition interval, this thermodynamic characteristic, calculated for the  $\gamma$ -Np-Mo solid solutions with both EMTO-CPA and FPLMTO-SQS methods, is positive

thus indicating a tendency towards phase separation. Notice that the heats of formation calculated with both EMT0-CPA and FPLMTO-SQS methods show an identical asymmetry with respect to the equiatomic composition, although for the  $\text{Np}_{75}\text{Mo}_{25}$  and  $\text{Np}_{50}\text{Mo}_{50}$  bcc alloys the FPLMTO-SQS calculations give some higher values of the heat of formation than the one calculated within EMT0-CPA formalism.

Fig. 1c presents results of EMT0-CPA and FPLMTO-SQS calculations of the heat of formation of the  $\gamma$ -Pu-Mo solid solutions at  $T = 0$  K. As in the case of the  $\gamma$ -Np-Mo solid solutions, the heat of formation of the  $\gamma$ -Pu-Mo solid solutions is positive through the entire composition interval, and both EMT0-CPA and FPLMTO-SQS results show an identical asymmetry with respect to the equiatomic composition, although for this system the FPLMTO-SQS calculations give some lower values of the heat of formation than one calculated within EMT0-CPA formalism.

Fig. 1d depicts results of EMT0-CPA and FPLMTO-SQS calculations of the heat of formation of the  $\gamma$ -Am-Mo solid solutions at  $T = 0$  K. There is a very good agreement between the results obtained from both theoretical methods with identical asymmetry with respect to the equiatomic composition. Generally speaking, Figs. 1a–d show a reasonable agreement between the two methodologies that are quite different both in regards to details of the electronic-structure codes but also the model of disorder (CPA and SQS). The level of consistency suggests a robustness of the density-functional theory approach for modeling these bcc-based X-Mo solid solutions.

Fig. 2 shows results of EMT0-CPA and FPLMTO-SQS calculations of the equilibrium atomic volume of the  $\gamma$ -X-Mo alloys at  $T = 0$  K. For the  $\gamma$ -U-Mo alloys (Fig. 2a), EMT0-CPA results, already presented in Ref. [2], show a slight positive deviation

from Vegard's law with a visible inflection around  $\text{U}_2\text{Mo}$  compound stoichiometry. As one can see from this figure, the positive deviation from Vegard's law for this system also follows from the FPLMTO-SQS model.

There is a significant positive deviation from Vegard's law for the  $\gamma\text{-Np-Mo}$  solid solution (Fig. 2b) that agrees well with the positive formation energy of these alloys. However, as was already pointed out in the previous paper [19], one should notice the calculated (EMTO-CPA and FPLMTO-SQS) value of the equilibrium volume of pure  $\gamma\text{-Np}$  is significantly smaller than observed experimentally [41]. The inaccuracy of the theoretical volume of  $\gamma\text{-Np}$  is consistent with previous calculations [42] and due to temperature effects of the actinide bcc phase that are difficult to model [43].

Finally, there is a negative deviation from Vegard's law for the equilibrium atomic volume calculated by both EMTO-CPA and FPLMTO-SQS methods for the  $\gamma\text{-Pu-Mo}$  and  $\gamma\text{-Am-Mo}$  alloys, shown in Fig. 2c and Fig. 2d, respectively, which, at first sight, contradicts the significant positive heat of formation associated with these systems. In the next section we will give our explanation of this unusual behavior of the equilibrium volume. We shall mention that our previous calculations also revealed a significant negative deviation from Vegard's law for the equilibrium atomic volume for the  $\gamma\text{-U-Am}$  and  $\gamma\text{-Am-Zr}$  alloys shown in Fig. 3a and Fig. 3b, respectively, even though the calculated positive heats of formation within the whole composition interval for these alloys were recently reported [11]. For example, EMTO-CPA calculations revealed that the heat of formation is equal to + 20.54 kJ/mole and + 8.86 kJ/mole for  $\gamma\text{-U}_{50}\text{Am}_{50}$ , and  $\gamma\text{-Am}_{50}\text{Zr}_{50}$  alloys, respectively [11].

#### 4. Discussion

Within the EMTO formalism [20, 21], the total-energy,  $E_{tot}$ , can be expressed as the sum of two contributions:  $E_{tot} = E_b + E_M$ , where  $E_b$  consists of all “local” (band-structure) contributions,  $E_b = E_s + E_{intra} + E_{xc}$ , including the kinetic energy of the non-interacting electron gas,  $E_s$ , the intra-cell electrostatic energy,  $E_{intra}$  (which is due to the electron-electron and electron-ion Coulomb interactions), and the exchange and correlation energy,  $E_{xc}$ . The remaining contribution,  $E_M$ , is the inter-cell Madelung energy.

In Table 1 we compare the results of our calculated heat of formation,  $\Delta E_{tot}$ , for bcc  $X_{50}Mo_{50}$  alloys. This Table also lists the energy contributions,  $\Delta E_b$ , and  $\Delta E_M$ , the equilibrium Wigner-Seitz (WS) radius,  $S_{WS}$ , (defined by equating the WS volume with the atomic volume), the screening constants,  $\alpha$  and  $\beta$ , and the charge transfer on the Mo atoms,  $\Delta Q_{Mo}$ , that is calculated by the LSGF method [31] for a 1024 atoms supercell that models the random equiatomic alloy. According to Ref. [29], the Madelung energy contribution to the heat of formation of a disordered  $A_cB_{1-c}$  alloy is proportional to

$$\left( -\alpha \frac{\Delta Q^2}{S_{WS}} \beta_c \right)^{1-c}, \text{ where } c \text{ is the concentration of the component 'A'. The}$$

Madelung energy contribution to the heat of formation of a disordered alloy is always negative and, as one can see from Table 1, the absolute value of this contribution for the  $U_{50}Mo_{50}$  alloy is  $\sim 1.26$ ,  $\sim 2.62$ , and  $\sim 5.13$  larger than for the  $Np_{50}Mo_{50}$ ,  $Pu_{50}Mo_{50}$ , and  $Am_{50}Mo_{50}$  alloys, respectively. Thus, as the value of the charge transfer on the Mo atoms,  $\Delta Q_{Mo}$ , decreases along the actinide row  $U \rightarrow Np \rightarrow Pu \rightarrow Am$ , the absolute value of the negative Madelung energy contribution to the total heat of formation of the

corresponding alloy decreases causing increase of the total heat of formation that is actually found by present calculations for the sequence of the U-Mo→Np-Mo→Pu-Mo→Am-Mo alloys. Even the band-structure contribution to the total heat of formation,  $E_B$ , is positive and  $\sim 1.15$  and  $\sim 1.61$  larger for the  $U_{50}Mo_{50}$  alloy than for the  $Np_{50}Mo_{50}$  and  $Pu_{50}Mo_{50}$  alloy, respectively, the negative Madelung energy contribution prevails in the case of the  $U_{50}Mo_{50}$  alloy resulting in a drop of the heat of formation of this alloy by a factor of  $\sim 1.88$  and  $\sim 3.54$  in comparison with the  $Np_{50}Mo_{50}$  and  $Pu_{50}Mo_{50}$  alloy, respectively. Comparing the positive band structure contribution for the  $U_{50}Mo_{50}$  and  $Am_{50}Mo_{50}$  alloys, one can find that this contribution is only  $\sim 1.16$  larger for the  $U_{50}Mo_{50}$  alloy than for the  $Am_{50}Mo_{50}$  alloy. The large negative Madelung energy contribution in the case of the  $U_{50}Mo_{50}$  alloy prevails and results in a drop of the heat of formation for this alloy by a factor of  $\sim 8.90$  in comparison with the  $Am_{50}Mo_{50}$  alloy.

In Fig. 4 we compared the results of EMTO-CPA calculations of the heat of formation of the bcc X-Mo solid solutions. The insert shows the charge transfer on the Mo atoms,  $\Delta Q_{Mo}$ , for the equiatomic alloy listed in Table 1. The system with the largest (smallest) charge transfer, U-Mo (Am-Mo), has the smallest (largest) heat of formation.

As we already mentioned in Section 2, the paramagnetic Pu-Mo and Am-Mo alloys have been modeled within the disordered local moment (DLM) approximation. Within the DLM approximation, a paramagnetic binary  $A_cB_{(1-c)}$  alloy is modeled by the random quaternary  $(A\uparrow-A\downarrow)_c(B\uparrow-B\downarrow)_{(1-c)}$  alloy with equal amount of spin up ( $\uparrow$ ) and spin down ( $\downarrow$ ) atoms [44]. In the case of the paramagnetic Pu-Mo and Am-Mo alloys, modeled within the DLM formalism, only Pu (Am) atoms possess the magnetic moment while the magnetic moment of Mo atoms is always equal to zero. That is why DLM description of

the Pu-Mo and Am-Mo alloys is simplified by the modeling of  $(\text{Pu}\uparrow\text{-Pu}\downarrow)_c(\text{Mo})_{(1-c)}$  and  $(\text{Am}\uparrow\text{-Am}\downarrow)_c(\text{Mo})_{(1-c)}$  alloy spin configurations, respectively.

Figs. 5a and 5b show the calculated (EMTO-CPA) concentration dependence of the absolute magnetic spin moment (no orbital component) of the bcc paramagnetic  $(\text{Pu}\uparrow\text{-Pu}\downarrow)_c(\text{Mo})_{(1-c)}$  and  $(\text{Am}\uparrow\text{-Am}\downarrow)_c(\text{Mo})_{(1-c)}$  alloys, respectively. It deviates negatively from a linear behavior for the  $\gamma$ -Pu-Mo system when concentration of Mo exceeds  $\sim 15$  at. %. For the  $\gamma$ -Am-Mo system this property displays the same behavior within the whole compositional range.

A similar tendency (negative deviation of the calculated absolute spin moment from linear behavior) was discovered in the DLM description of the paramagnetic Fe-Cr alloys [45, 46]. The DLM model also revealed a significant negative deviation of the equilibrium atomic volume from the Vegard's law in this system (e.g., see Ref. [47], Fig. 1a) that is accompanied with a positive heat of formation [45-47]. The believed reason is that the equilibrium volume is sensitive to magnetism, which gives rise to this counterintuitive behavior. A net magnetic itinerant spin moment (in any configuration) implies spin polarization of the responsible bands (here  $5f$  bands). Generally, this can lead to a reduction of bonding electrons (thus expanding the volume) or even disrupt the systematics of the crystal structures, as in the case of the magnetic  $3d$  transition metals [48]. This then explains why the calculated equilibrium volume deviates from a linear behavior (the Vegard's law) with alloying in a similar fashion as the absolute magnetic spin moment does. We thus conclude that the negative deviation of the absolute magnetic spin moment from linear behavior in the DLM paramagnetic binary  $A_cB_{(1-c)}$  alloys causes the negative deviation of the equilibrium atomic volume from the Vegard's law in these

alloys even if the heat of formation of these alloys remains positive. This hypothesis accounts for the negative deviation of the equilibrium atomic volume from the Vegard's law for the DLM  $\gamma$ -Pu-Mo and  $\gamma$ -Am-Mo alloys shown in Figs. 2c and 2d, respectively, although both alloys have a positive heat of formation. Two other alloys studied in this paper, U-Mo and Np-Mo, are non-magnetic and their positive heat of formation is accompanied with the positive deviation of the equilibrium volume from the Vegard's law in these alloys – a scenario shown in most textbooks.

In order to support our hypothesis that magnetism plays a decisive role in determining the character of the concentration behavior of the equilibrium atomic volume of paramagnetic alloys, we plot, in Fig. 5c, the concentration dependence of the calculated (EMTO-CPA) magnitude of the spin moment of the bcc paramagnetic Pu-Am system that is represented within DLM formalism by  $(\text{Pu}\uparrow\text{-Pu}\downarrow)_c(\text{Am}\uparrow\text{-Am}\downarrow)_{(1-c)}$  spin configuration. In the case of paramagnetic  $\gamma$ -Pu-Am alloys both Pu and Am atoms possess a magnetic moment. The calculated absolute magnetic moment of the  $\gamma$ -Pu-Am alloys shows a positive deviation from linear behavior when the concentration of Am exceeds  $\sim 15$  at. % and this behavior drives the positive deviation of the equilibrium atomic volume from the Vegard's law in these alloys that is shown in Fig. 6. One should mention that in addition to results of the EMTO-CPA calculations, already presented in Ref. [19], Fig. 6 also shows results of FPLMTO-SQS calculations for this system that also indicate a positive deviation of the equilibrium atomic volume from the Vegard's law. The positive deviation of the equilibrium atomic volume from the Vegard's law in the DLM paramagnetic  $\gamma\text{-Pu}_c\text{Am}_{(1-c)}$  alloys is accompanied by a positive heat of formation through the entire composition interval [19, 49].

## 5. Conclusion

In the present paper *ab initio* results of the ground-state properties are obtained for the bcc Np-Mo, Pu-Mo, and Am-Mo alloys to understand the effectiveness of first-principles methods in describing actinide alloys. The reason for an increase of the heat of formation along the sequence of the U-Mo→Np-Mo→Pu-Mo→Am-Mo alloys is explained. The physical origin of the deviation of the equilibrium volume from the Vegard's law in paramagnetic alloys is discussed. Together with our *ab initio* results obtained previously for U-Mo, U-Am, Pu-U, Pu-Np, and Pu-Am alloys [2, 9, 11, 19, 49] these new results will be used to build a thermodynamic database for U-TRU-Mo alloys that are considered to be very promising fuels for fast breeder reactors [4, 50-56].

## Acknowledgements

This work was performed under the auspices of the U.S. Department of Energy by Lawrence Livermore National Laboratory under contract DE-AC52-07NA27344. Work at LLNL was funded by the Laboratory Directed Research and Development Program under project tracking code 12-SI-008. Financial support from the DOE-NE NEAMS Program is gratefully acknowledged. A.L. would like to acknowledge Profs. A.V. Ruban and L. Vitos for helpful discussion.

## References:

1. A. Landa, P. Söderlind, P.E.A. Turchi, L. Vitos, A. Ruban, J. Nucl. Mater. 385 (2009) 68-71.



2. A. Landa, P. Söderlind, P.E.A. Turchi, J. Nucl. Mater. 414 (2011) 132-137.
3. G.L. Hofman, L.C. Walters, T.H. Bauer, Progr. Nucl. Energy 31 (1/2) (1997) 83-110.
4. Y.-S. Kim, G.L. Hofman, A.M. Yacout, T.-K. Kim, in: T. Okazaki, J. Bouchard, T. Takeda, Y. Oka (Eds.), Proceedings of International Conference on Fast Reactors and Related Fuel Cycles (FR09), Challenges and Opportunities, I A E A-CN-176, Kyoto, Japan, (2009) pp. 1-9.
5. M. Kurata, T. Inoue, C. Sari, J. Nucl. Mater. 208 (1994) 144-158.
6. Y.-S. Kim, G.L. Hofman, S.L. Hayes, Y.-H. Sohn, J. Nucl. Mater. 327 (2004) 27-36.
7. Y.-S. Kim, G.L. Hofman, A.M. Yacout, J. Nucl. Mater. 392 (2009) 164-170.
8. G.L. Hofman, S.L. Hayes, M.C. Petri, J. Nucl. Mater. 227 (1996) 277-286.
9. A. Landa, P. Söderlind, P.E.A. Turchi, L. Vitos, A. Ruban, J. Nucl. Mater. 393 (2009) 141-145.
10. S. Bajaj, A. Garay, A. Landa, P. Söderlind, P.E.A. Turchi, R. Arróyave, J. Nucl. Mater. 409 (2011) 1-8.
11. A. Landa, P. Söderlind, B. Grabowski, P.E.A. Turchi, A. Ruban, L. Vitos, in: D. Andersson, T. Durakewicz, C.H Booth, M. Stan, P.C. Burns, V. Tikare, R. Caciuffo, S.-W. Yu, R. Devanathan (Eds.), Actinides and Nuclear Energy Materials, Material Research Society, vol. 1444, Cambridge University Press, Cambridge, 2012, pp. 67-78.

12. P.E.A. Turchi, I.A. Abrikosov, B. Burton, S.G. Fries, G. Grimvall, L. Kauffman, P. Korzhavyi, V. Rao Manga, M. Ohno, A. Pisch, A. Scott, W. Zhang, CALPHAD 31 (2007) 4-27.
13. M. Kurata, T. Ogata, K. Nakamura, T. Ogawa, J. Alloys Comp. 271/273 (1998) 636-640.
14. M. Kurata, CALPHAD 23 (1999) 315-337.
15. L. Brewer, R.H. Lamoreaux, in: (T.B. Massalski Ed.), Binary Alloys Phase Diagrams, second ed., vol. 3, ASM International, Materials Park, Ohio, 1990, p. 2638-2640.
16. L. Brewer, R.H. Lamoreaux, in: (T.B. Massalski Ed.), Binary Alloys Phase Diagrams, second ed., vol. 3, ASM International, Materials Park, Ohio, 1990, p. 2650-2653.
17. L. Brewer, R.H. Lamoreaux, in: (T.B. Massalski Ed.), Binary Alloys Phase Diagrams, second ed., vol. 1, ASM International, Materials Park, Ohio, 1990, p. 249-250.
18. L. Brewer, R.H. Lamoreaux, At. Energy Rev. № (7) (1980) 11-194 (Spec. Issue).
19. A. Landa, P. Söderlind, P.E.A. Turchi, L. Vitos, O.E. Peil, A.V. Ruban, J. Nucl. Mater. 408 (2011) 61-66.
20. L. Vitos, Phys. Rev B 64 (2001) 014107-1-014107-11.
21. L. Vitos, Computational Quantum Mechanics for Materials Engineers: The EMT0 Method and Application, Springer-Verlag, London, 2007.

22. J. Kollar, L. Vitos, H.L. Skriver, in: H. Dreyssé (Ed.), *Electronic Structure and Physical Properties of Solids: The Uses of the LMTO Method*, Lecture Notes in Physics, Springer-Verlag, Berlin, 2000, pp. 85-113.
23. J.P. Perdew, K. Burke, M. Ernzerhof, *Phys. Rev. Lett.* 77 (1996) 3865-3868.
24. D.J. Chadi, M.L. Cohen, *Phys. Rev. B* 8 (1973) 5747-5753; S. Froyen, *Phys. Rev. B* 39 (1989) 3168-3172.
25. L.V. Pourovskii, A.V. Ruban, L. Vitos, H. Ebert, B. Johansson, I.A. Abrikosov, *Phys. Rev. B* 71 (2005) 094415-1-094415-10.
26. J.S. Faulkner, *Prog. Mater. Sci.* 27 (1982) 1-187.
27. L. Vitos, I.A. Abrikosov, B. Johansson, *Phys. Rev. Lett.* 87 (2001) 156401-1-156401-4.
28. A.V. Ruban, H.L. Skriver, *Phys. Rev. B* 66 (2002) 024201-1-024201-15.
29. A.V. Ruban, S.I. Simak, P.A. Korzhavyi, H.L. Skriver, *Phys. Rev. B* 66 (2002) 024202-1-024202-12.
30. A.V. Ruban, S.I. Simak, S. Shallcross, H.L. Skriver, *Phys. Rev. B* 67 (2003) 214302-1-214302-12.
31. I.A. Abrikosov, S.I. Simak, B. Johansson, A.V. Ruban, H.L. Skriver, *Phys. Rev. B* 56 (1997) 9319-9334.
32. P. Söderlind, A. Landa, B. Sadigh, *Phys. Rev. B* 66 (2002) 205109-1-205109-6.
33. A. Landa, P. Söderlind, *J. Alloys Comp.* 354 (2003) 99-103.
34. F.D. Murnaghan, *Proc. Natl. Acad. Sci. U.S.A.* 30 (1944) 244-247.
35. O.K. Andersen, *Phys. Rev. B* 12 (1975) 3060-3083.

36. A. Landa, P. Söderlind, in: J.L. Sarrao, A.J. Schwartz, M.R. Antonio, P.C. Burns, R.G. Haire, H. Nitsche (Eds.), *Actinides 2005-Basic Science, Applications and Technology*, Material Research Society, vol. 893, Springer-Verlag, Berlin, 2006, pp. 51-56.
37. J.M. Wills, M. Alouani, P. Andersson, A. Delin, O. Eriksson, O. Grechnev, *Full-Potential Electronic Structure Method*, Springer-Verlag, Berlin, 2010.
38. A. Zunger, S.H. Wei, L.G. Ferreira, J.E. Bernard, *Phys. Rev. Lett.* 65 (1990) 353-356.
39. P. Söderlind, B. Sadigh, *Phys. Rev. Lett.* 92 (2004) 185702-1-185702-4; P. Söderlind, *Europhys. Lett.* 55 (2001) 525-531.
40. X. Zhang, Y. F. Cui, G. L. Xu, W.J. Zhu, H.S. Liu, B.Y. Yin, Z.P. Jin, *J. Nucl. Mater.* 402 (2010) 15-24.
41. P.G. Mardon, J. H. Pearce, J.A.C. Marples, *J. Less-Common Met.* 3 (1961) 281-292.
42. P. Söderlind, B. Johansson, O. Eriksson, *Phys. Rev. B* 52 (1995) 1631-1639.
43. P. Söderlind, B. Grabowski, L. Yang, A. Landa, T. Björkman, P. Souvatzis, O. Eriksson, *Phys. Rev. B* 85 (2012) 060301-1-060301-4(R).
44. B.L. Györffy, A.J. Pindor, J. Staunton, G.M. Stocks, H. Winter, *J. Phys. F* 15 (1985) 1337-1386.
45. P. Olsson, I.A. Abrikosov, L. Vitos, J. Wallenius, *J. Nucl. Mater.* 321 (2003) 84-90.
46. P. Olsson, I.A. Abrikosov, J. Wallenius, *Phys. Rev. B* 73 (2006) 104416-1-104416-8.

47. A.V. Ponomareva, A.V. Ruban, O.Yu. Vekilova, S.I. Simak, I.A. Abrikosov, Phys. Rev. B 84 (2011) 094422-1-094422-6.
48. P. Söderlind, R. Ahuja, O. Eriksson, B. Johansson, J.M. Wills, Phys. Rev. B 50 (1994) 5918-5927.
49. P.E.A. Turchi, A.I. Landa, P. Söderlind, J. Nucl. Mater. 418 (2011) 165-173.
50. D.M. Wachs, Nuclear Engineering International, 08 March 2010, pp. 1-6.
51. E. Perez, B. Yao, D.D. Keiser Jr., Y.-H. Sohn, J. Nucl. Mater. 402 (2010) 8-14.
52. R.M. Hengstler, L. Beck, H. Breitzkreutz, C. Jarousse, R. Jungwirth, W. Petry, W. Schmid, J. Schneider, N. Weischalla, J. Nucl. Mater. 402 (2010) 74-80.
53. D.E. Burkes, C.A. Papesch, A.P. Maddison, T. Hartmann, F.J. Rice, J. Nucl. Mater. 403 (2010) 160-166.
54. S. Neogy, M.T. Saify, S.K. Jha, D. Srivastava, M.M. Hussain, G.K. Dey, R.P. Singh, J. Nucl. Mater. 422 (2012) 77-85.
55. Y.-S. Kim, G.L. Hofman, J. Nucl. Mater. 425 (2012) 181-187.
56. D.D. Keiser Jr., J.-F. Jue, A.B. Robinson, P. Medvedev, J. Gan, B.D. Miller, D.M. Wachs, G.A. Moore, C.R. Clark, M. K. Meyer, M. Ross Finlay, J. Nucl. Mater. 425 (2012) 156-172.

**Table 1.**

Equilibrium Wigner-Seitz radius,  $S_{WS}$ , (in a.u., 1 a.u.= 0.0529 nm), screening constants,  $\alpha$  and  $\beta$ , charge transfer on the Mo atoms,  $\Delta Q_{Mo}$ , contributions,  $\Delta E_b$  and  $\Delta E_M$ , to the heat of formation,  $\Delta E_{tot}$ , (in kJ/mole) of the bcc  $U_{50}Mo_{50}$ ,  $Np_{50}Mo_{50}$ ,  $Pu_{50}Mo_{50}$ , and  $Am_{50}Mo_{50}$  alloys.

| Alloy            | $S_{WS}$ | $\alpha$ | $\beta$ | $\Delta Q_{Mo}$ | $\Delta E_b$ | $\Delta E_M$ | $\Delta E_{tot}$ |
|------------------|----------|----------|---------|-----------------|--------------|--------------|------------------|
| $U_{50}Mo_{50}$  | 3.1274   | 0.725    | 1.088   | 0.440           | 74.5648      | - 68.8681    | 5.6967           |
| $Np_{50}Mo_{50}$ | 3.0629   | 0.726    | 1.083   | 0.380           | 65.0899      | - 54.4927    | 10.5972          |
| $Pu_{50}Mo_{50}$ | 3.0921   | 0.655    | 0.953   | 0.318           | 46.4297      | - 26.2651    | 20.1646          |
| $Am_{50}Mo_{50}$ | 3.1725   | 0.585    | 0.802   | 0.280           | 64.1060      | -13. 4138    | 50.6922          |

### Captions.

Figure 1. Heat of formation (in kJ/mole) versus composition for the  $\gamma$ -U-Mo (a),  $\gamma$ -Np-Mo (b),  $\gamma$ -Pu-Mo (c), and  $\gamma$ -Am-Mo (d) alloys ( $T = 0$  K).

Figure 2. Atomic volume (in nm<sup>3</sup>) versus composition for the  $\gamma$ -U-Mo (a),  $\gamma$ -Np-Mo (b),  $\gamma$ -Pu-Mo (c), and  $\gamma$ -Am-Mo (d) alloys ( $T = 0$  K).

Figure 3. Atomic volume (in nm<sup>3</sup>) versus composition for the  $\gamma$ -U-Am (a) and  $\gamma$ -Am-Zr (b) alloys ( $T = 0$  K).

Figure 4. Heat of formation (in kJ/mole) versus composition for the bcc U-Mo, Np-Mo, Pu-Mo, and Am-Mo alloys ( $T = 0$  K). The insert shows the charge transfer on the Mo atoms calculated by the LSGF method [31] for a supercell that models the random equiatomic alloy.

Figure 5. Absolute magnetic moment (in  $\mu$ B/atom) versus composition for the  $\gamma$ -Pu-Mo (a),  $\gamma$ -Am-Mo (b), and  $\gamma$ -Pu-Am (c) alloys ( $T = 0$  K).

Figure 6. Atomic volume (in nm<sup>3</sup>) versus composition for the  $\gamma$ -Pu-Am alloys.

Figures.

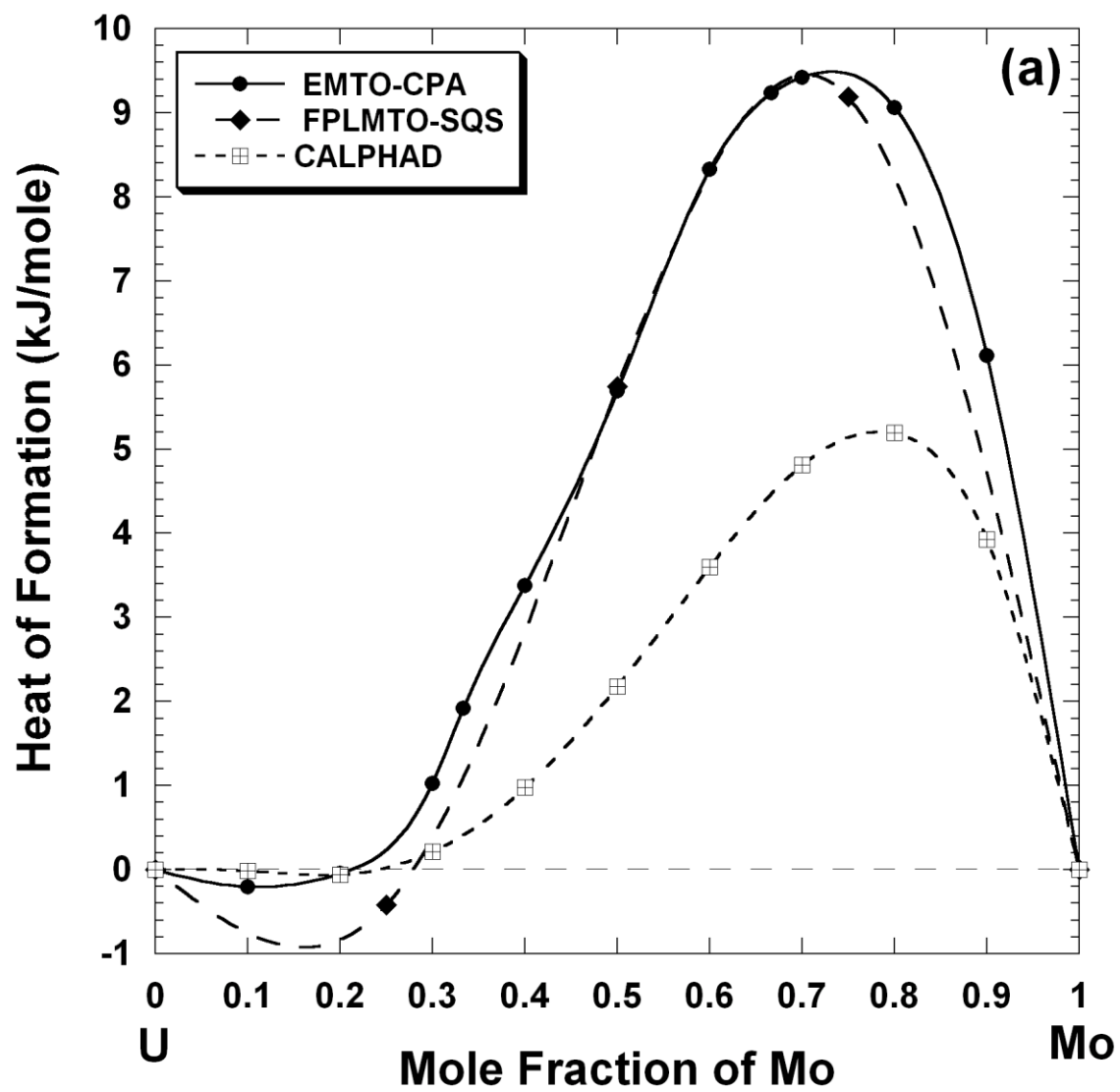


Figure 1a.



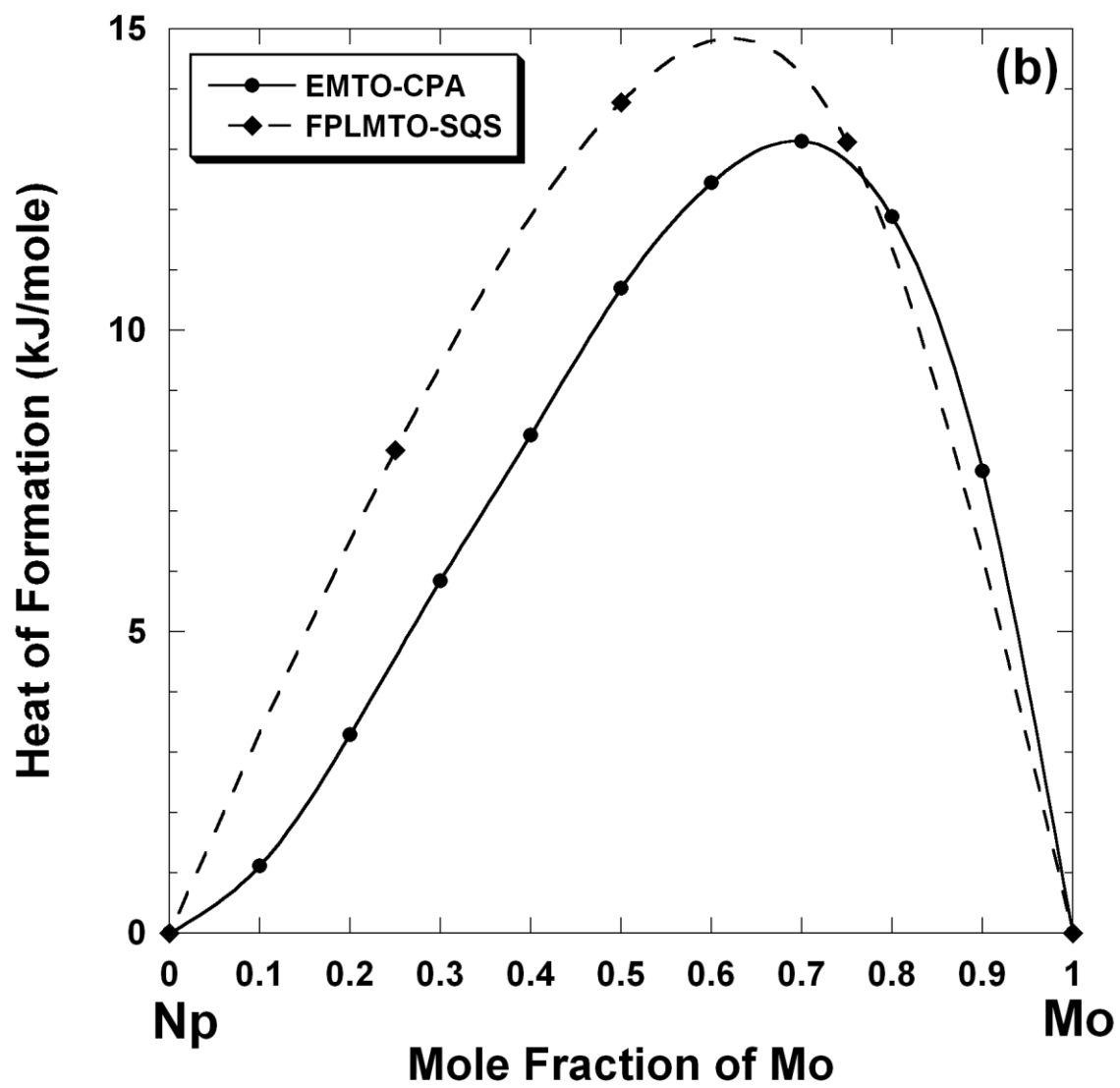


Figure 1b.

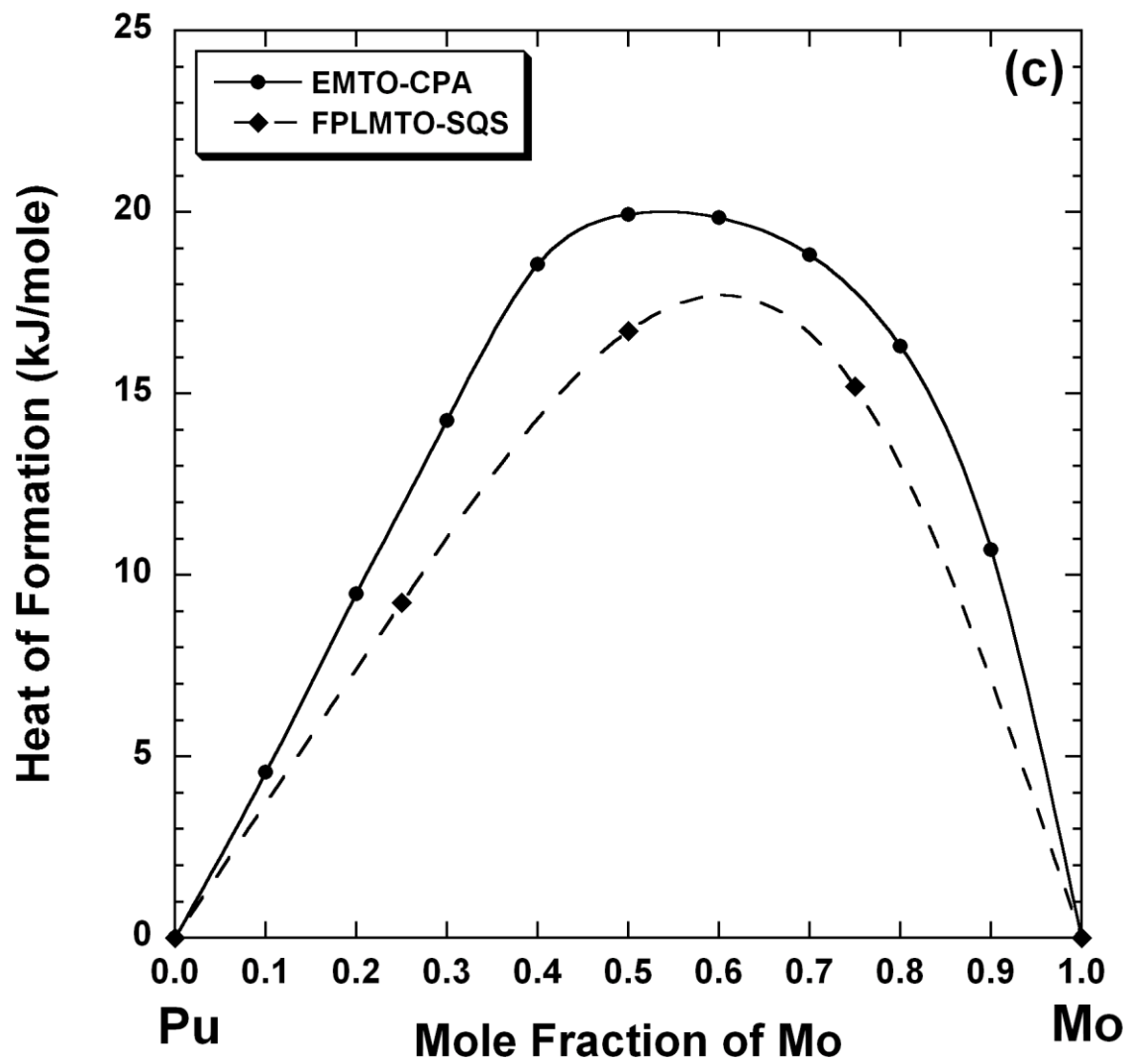


Figure 1c.

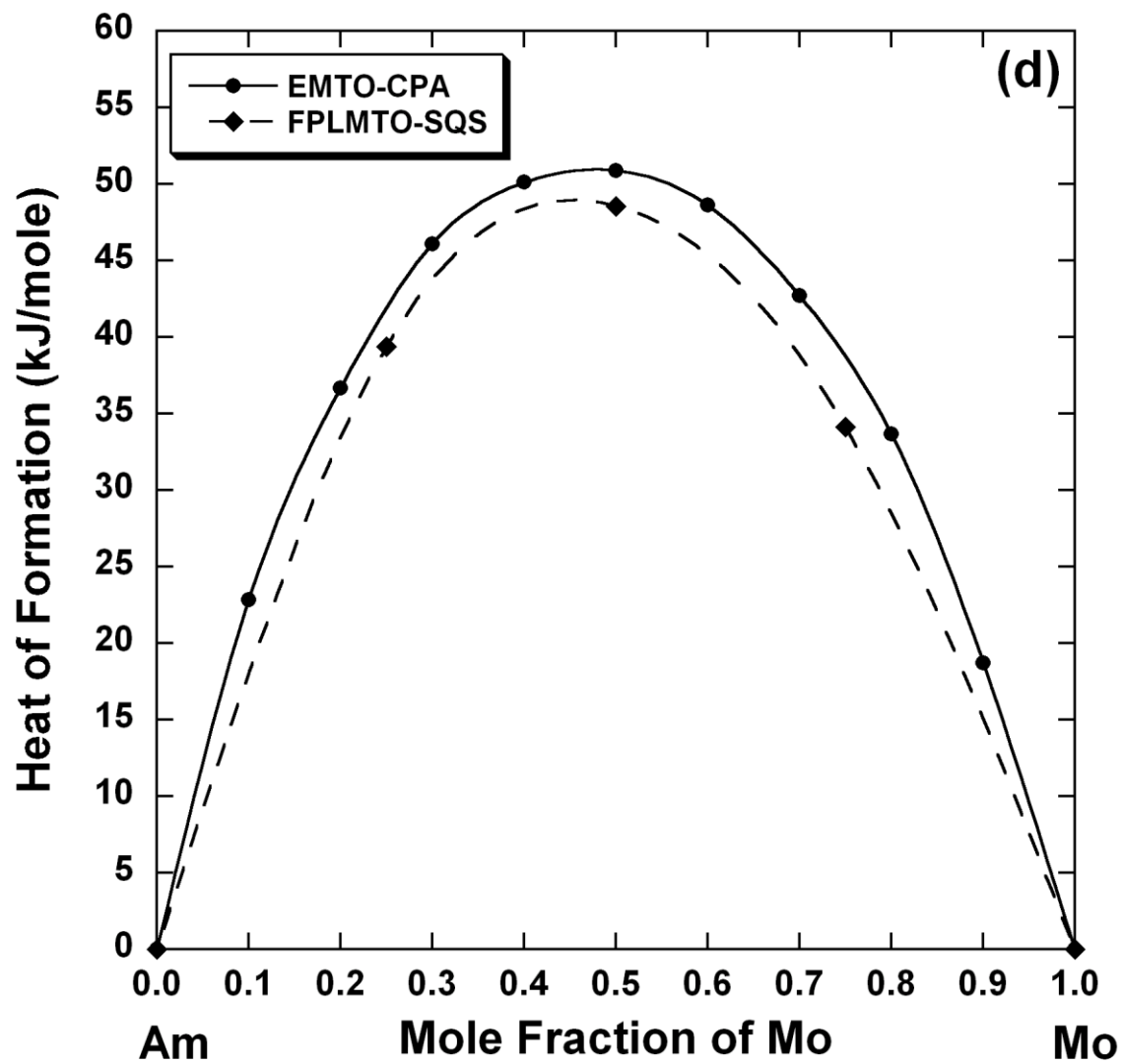


Figure 1d.

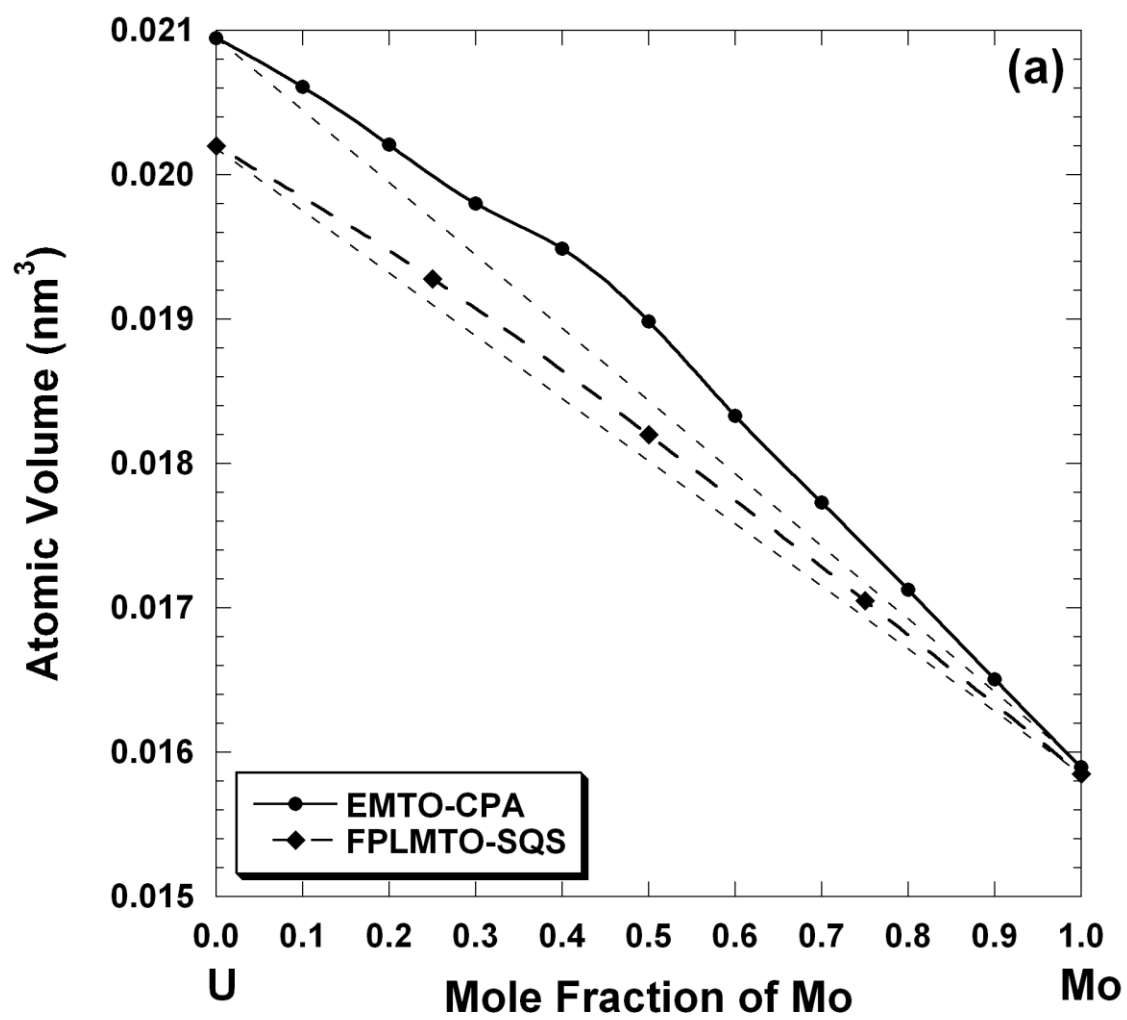


Figure 2a.

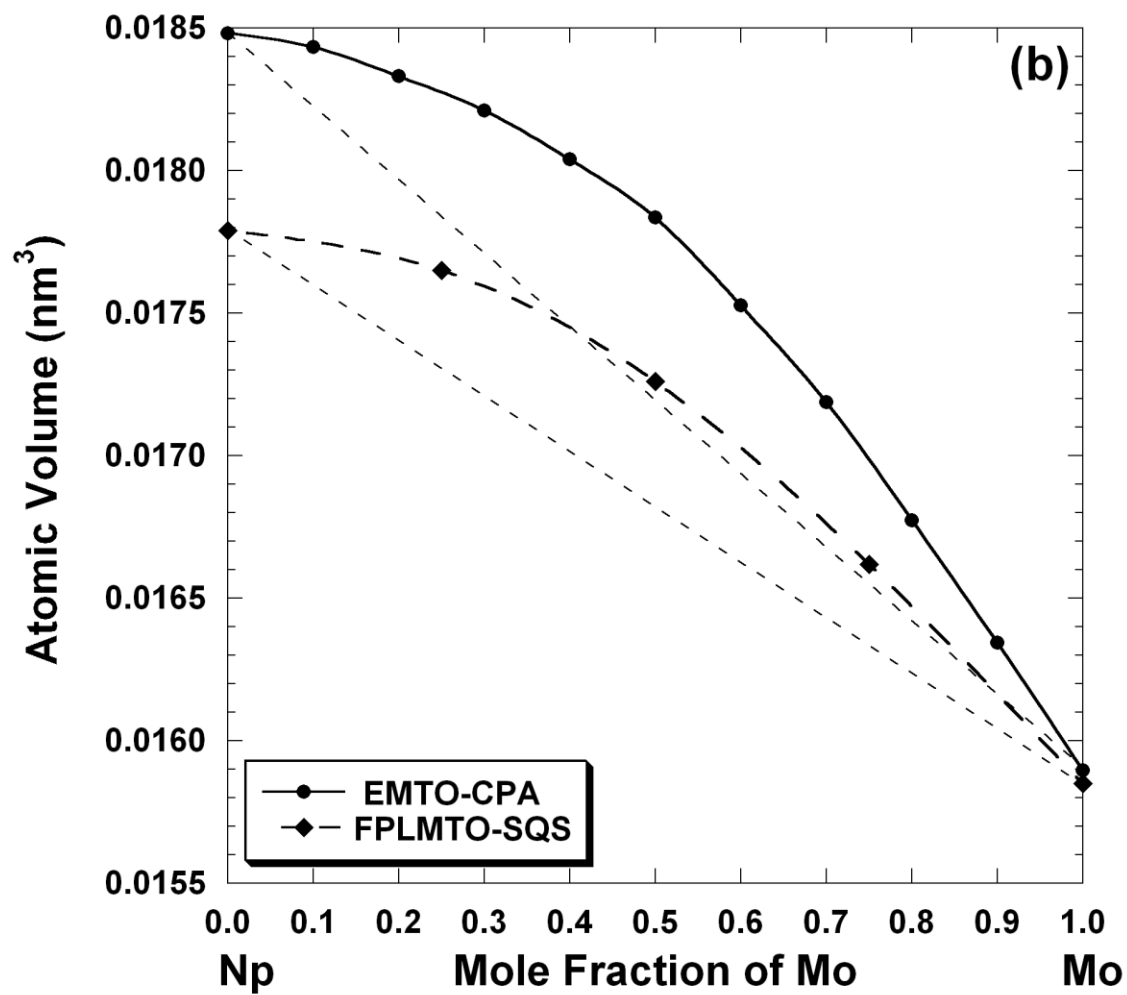


Figure 2b.

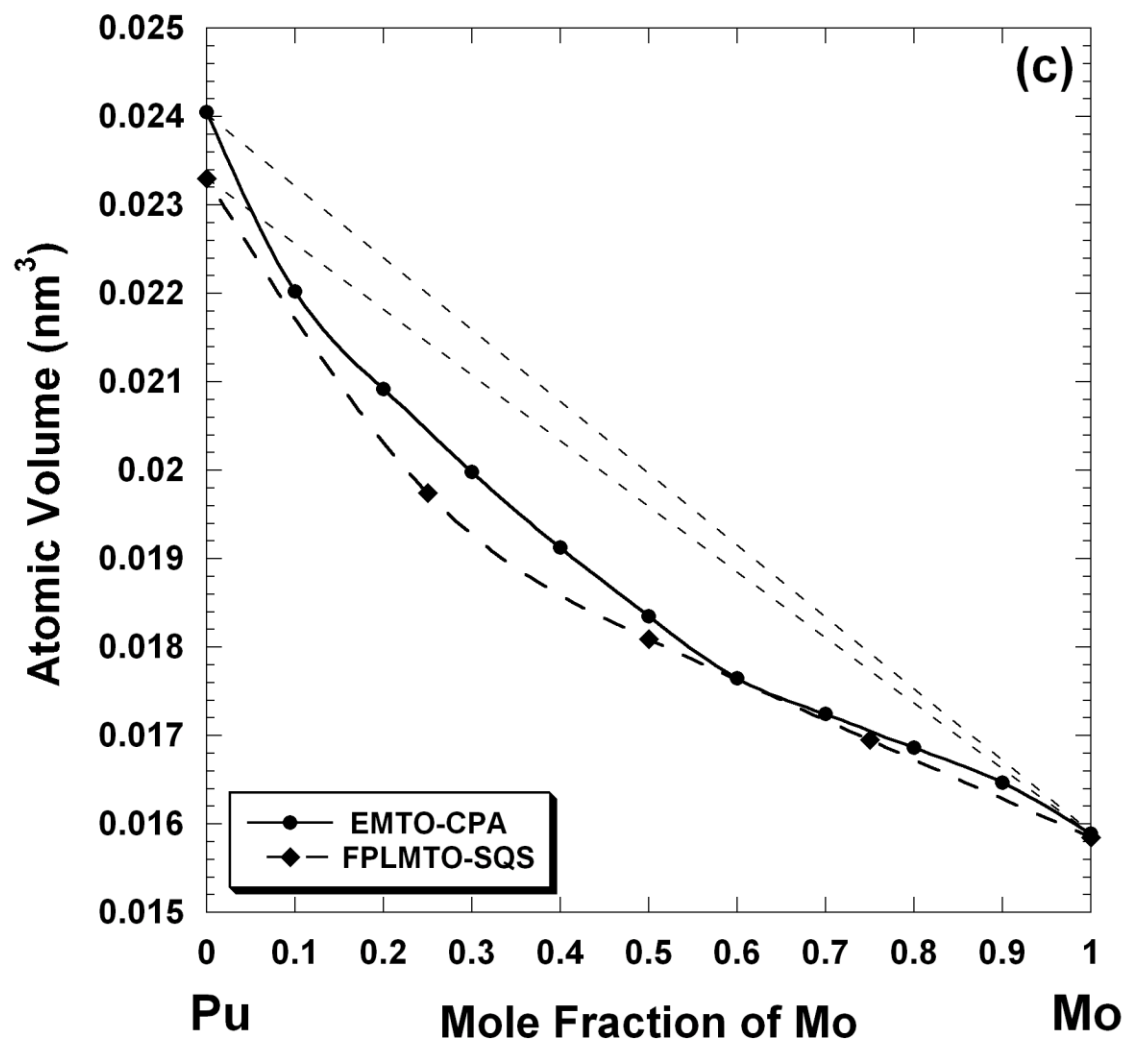


Figure 2c.

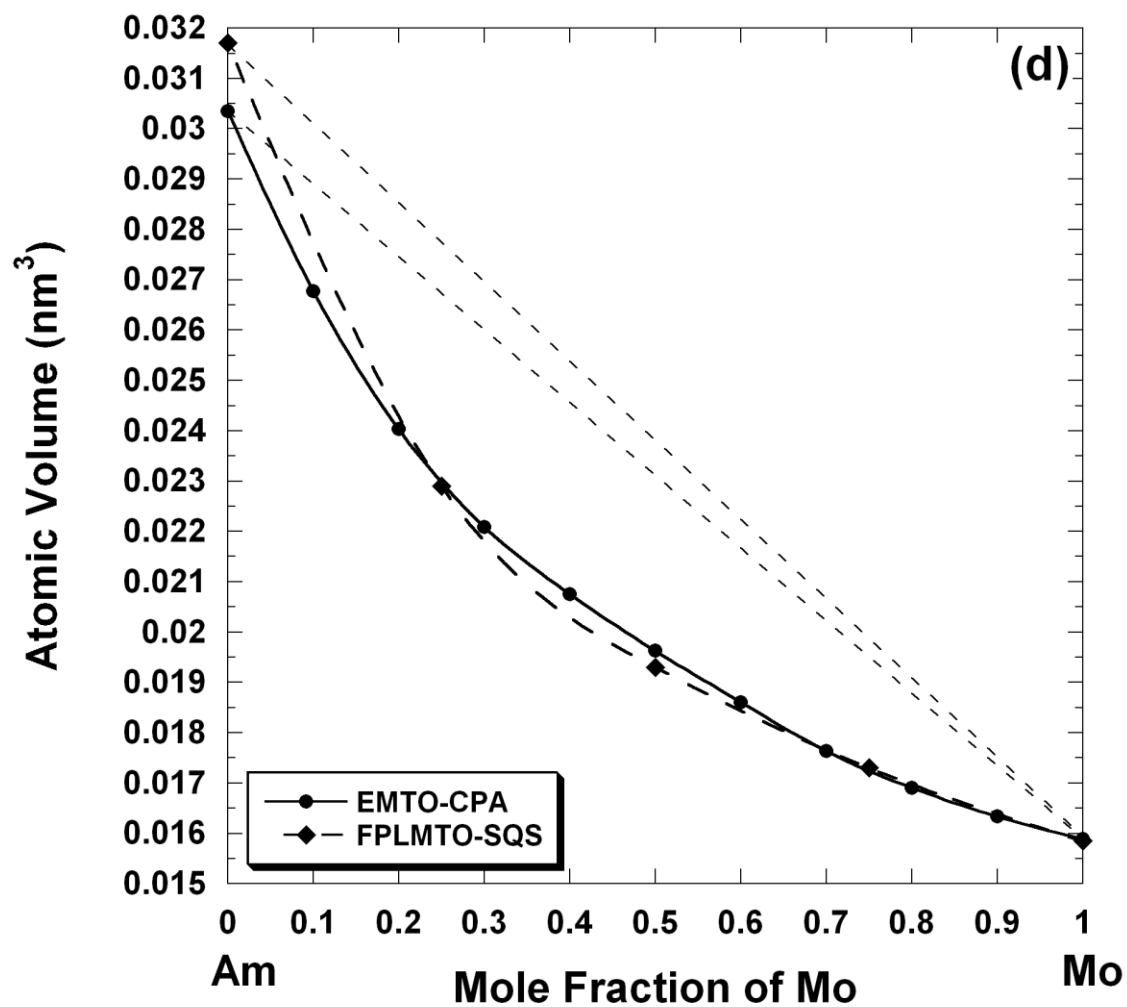


Figure 2d.

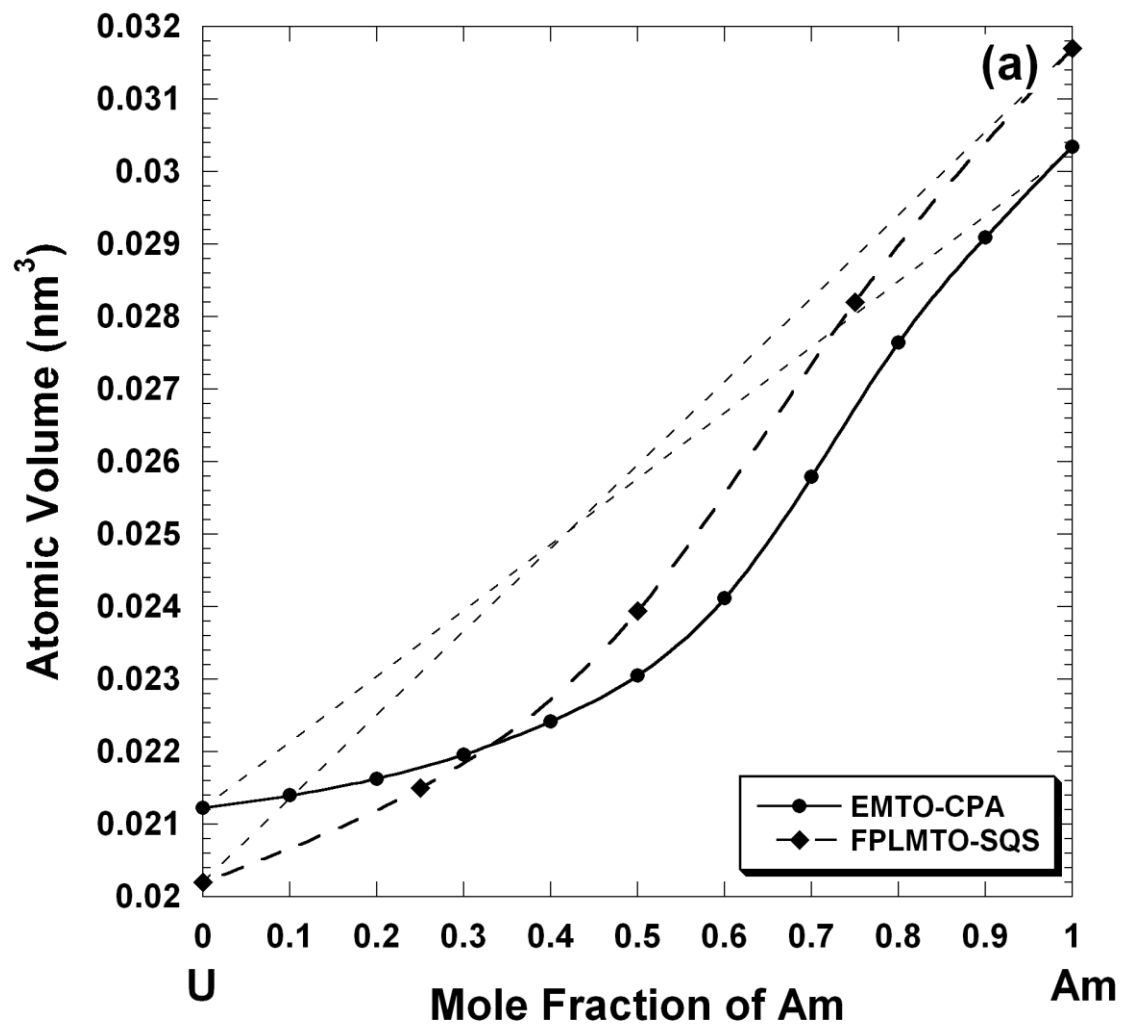


Figure 3a.



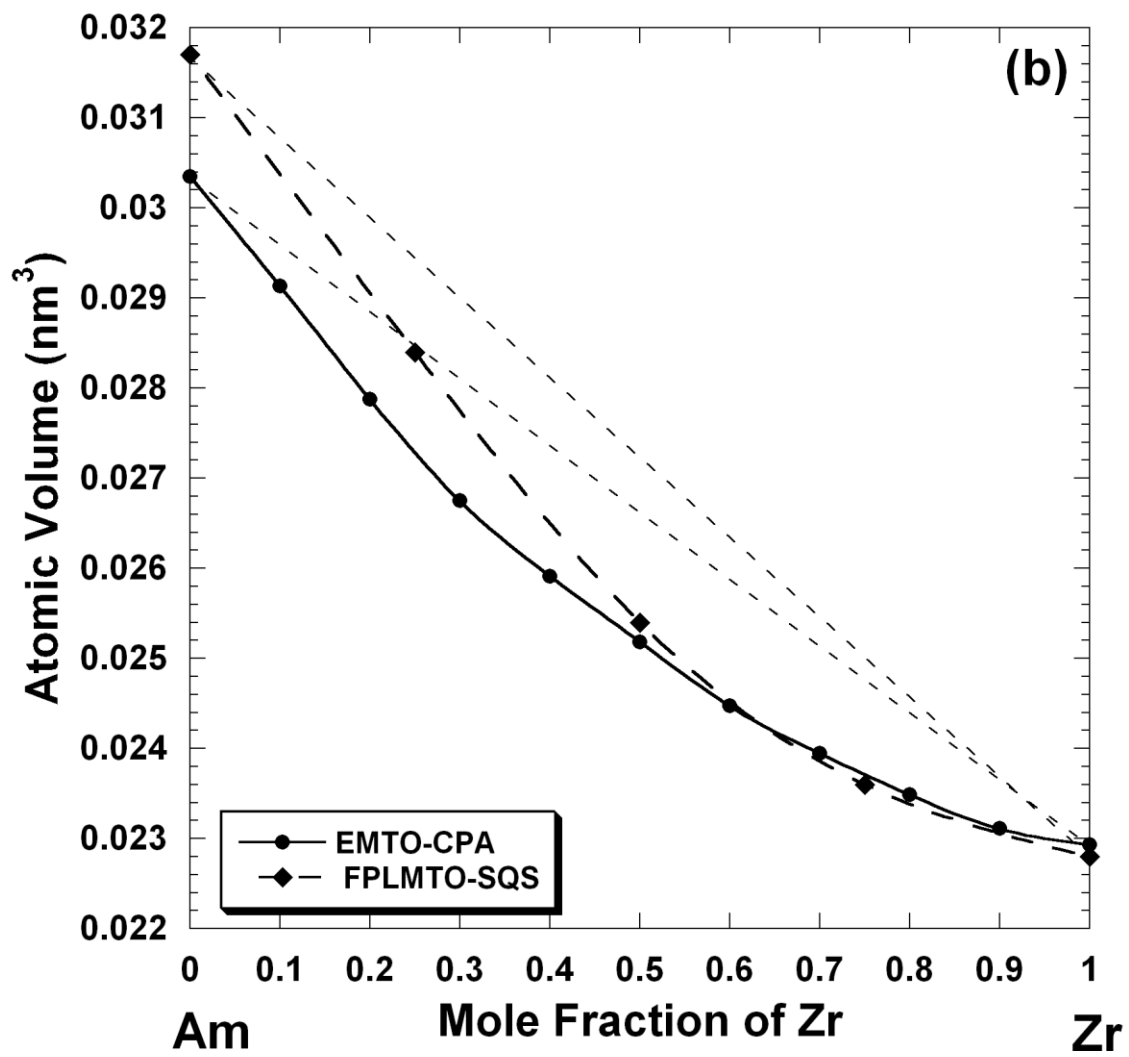


Figure 3b.

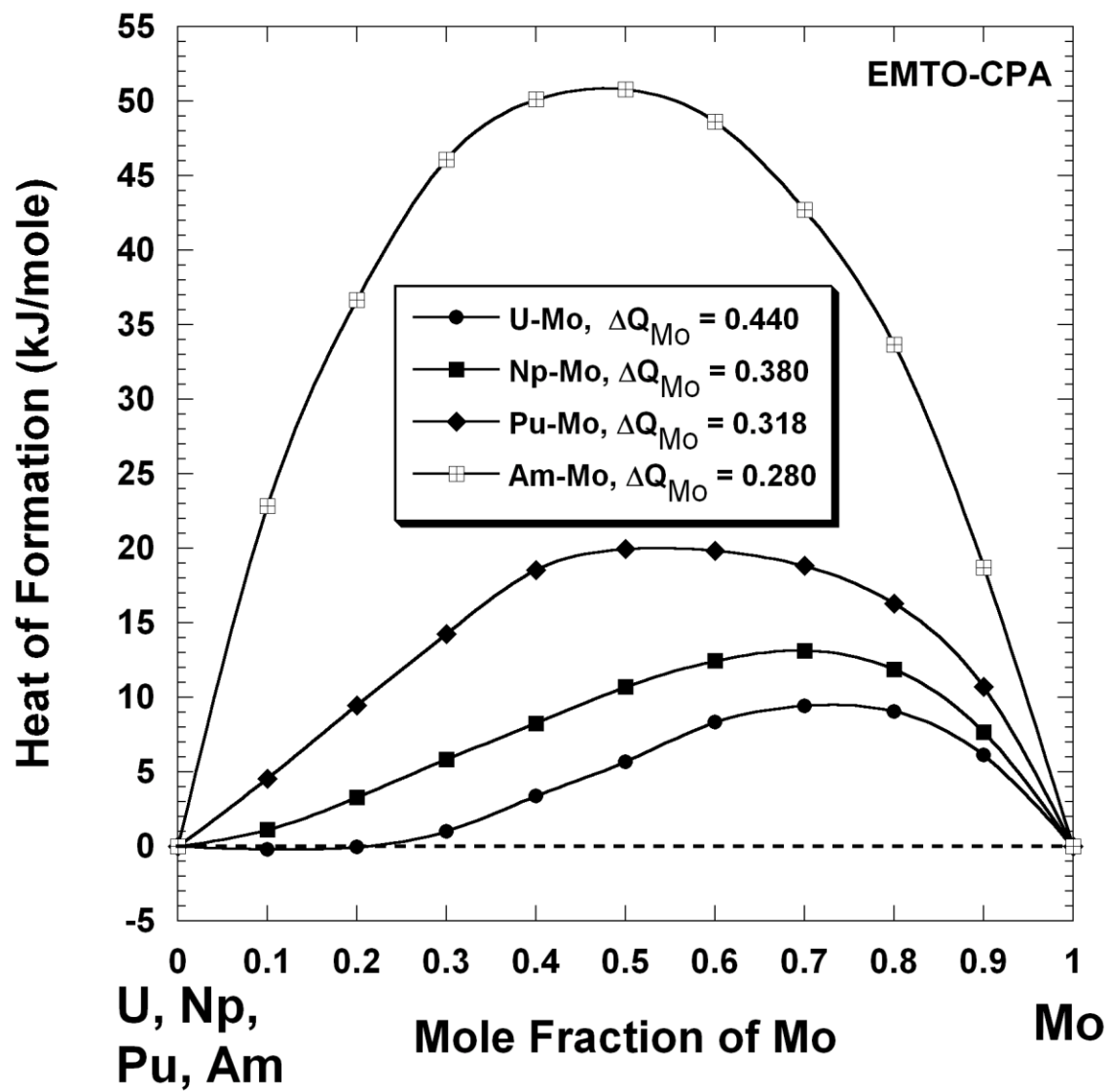


Figure 4.

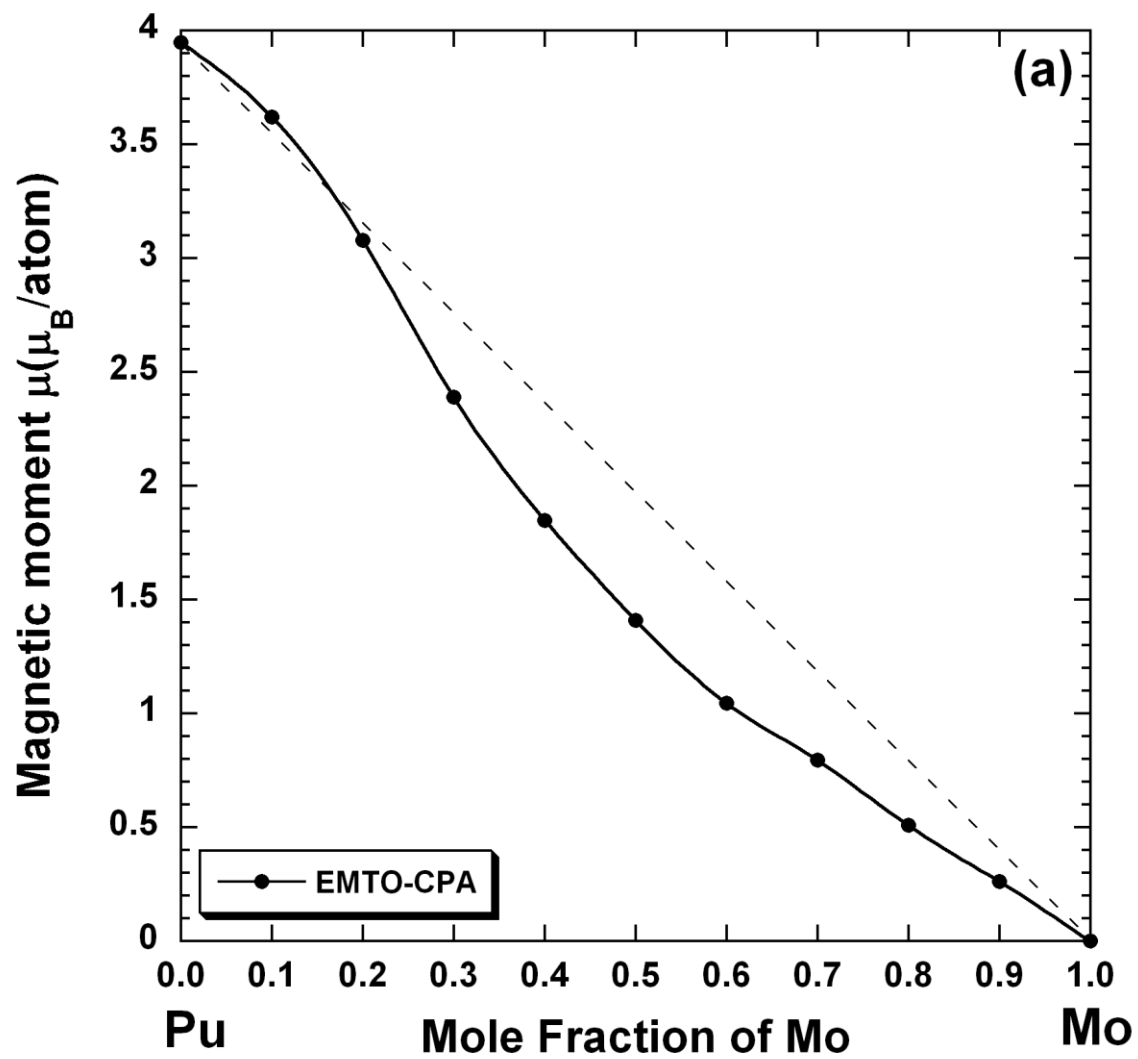


Figure 5a.

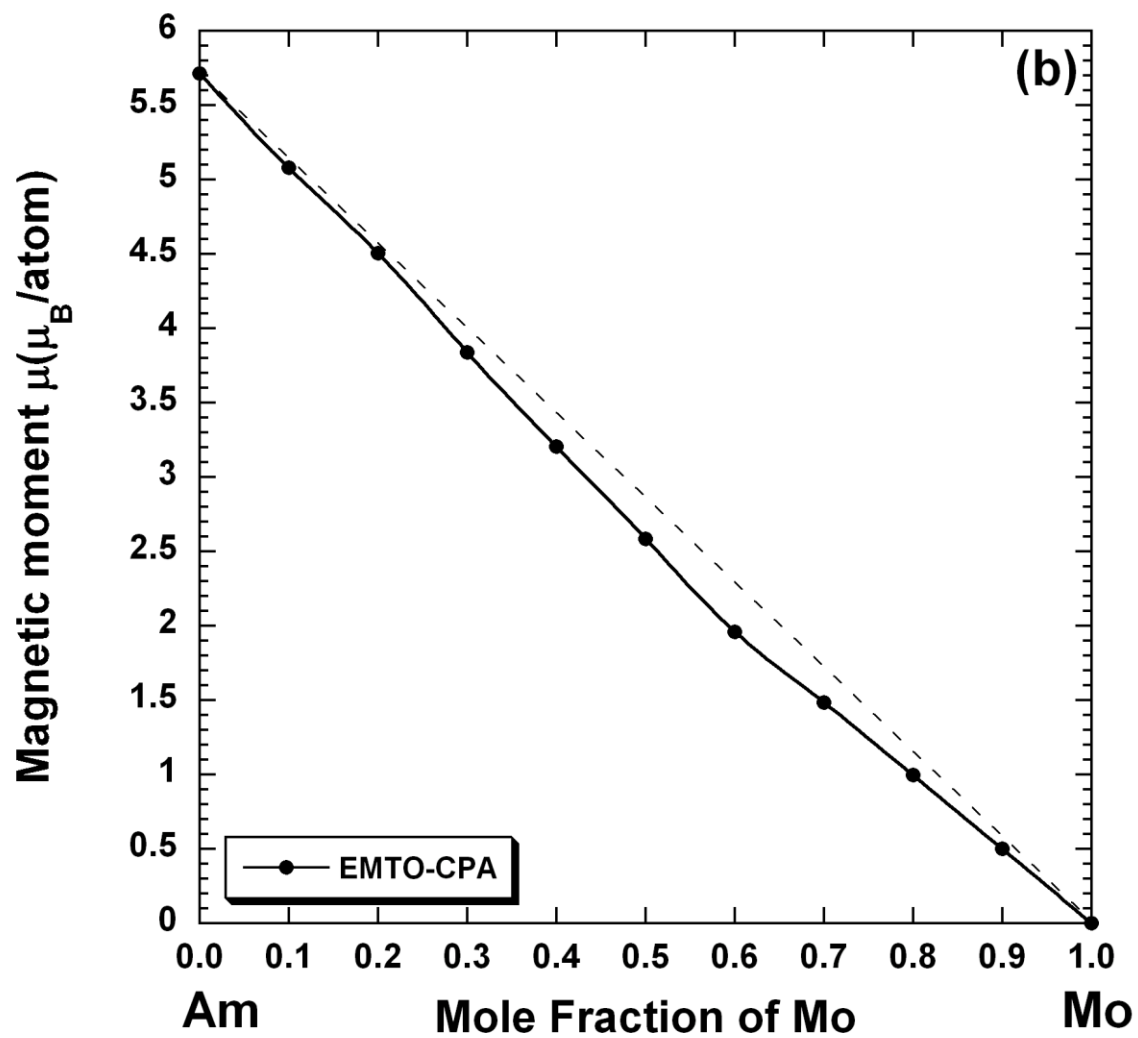


Figure 5b.

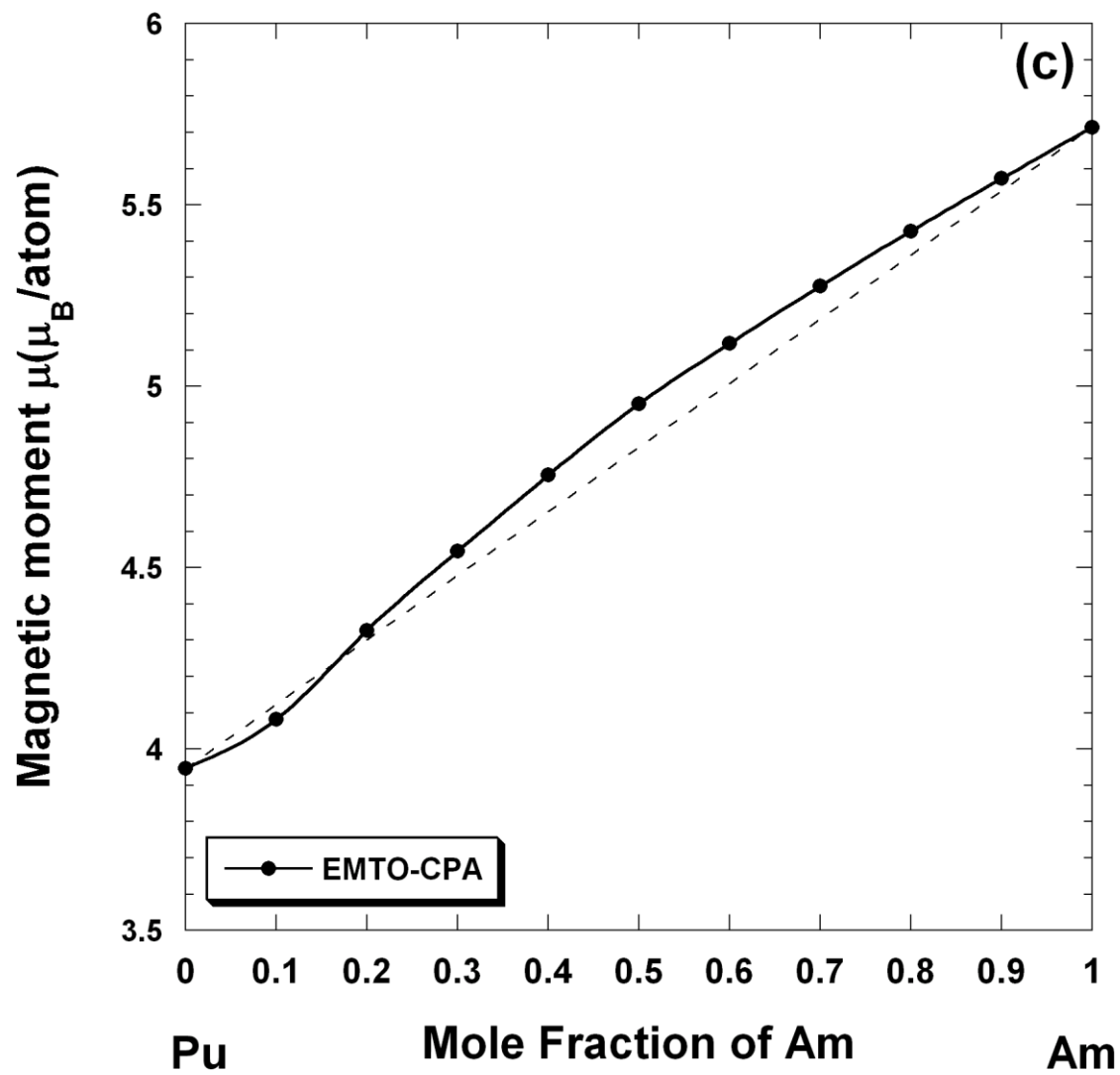


Figure 5c.

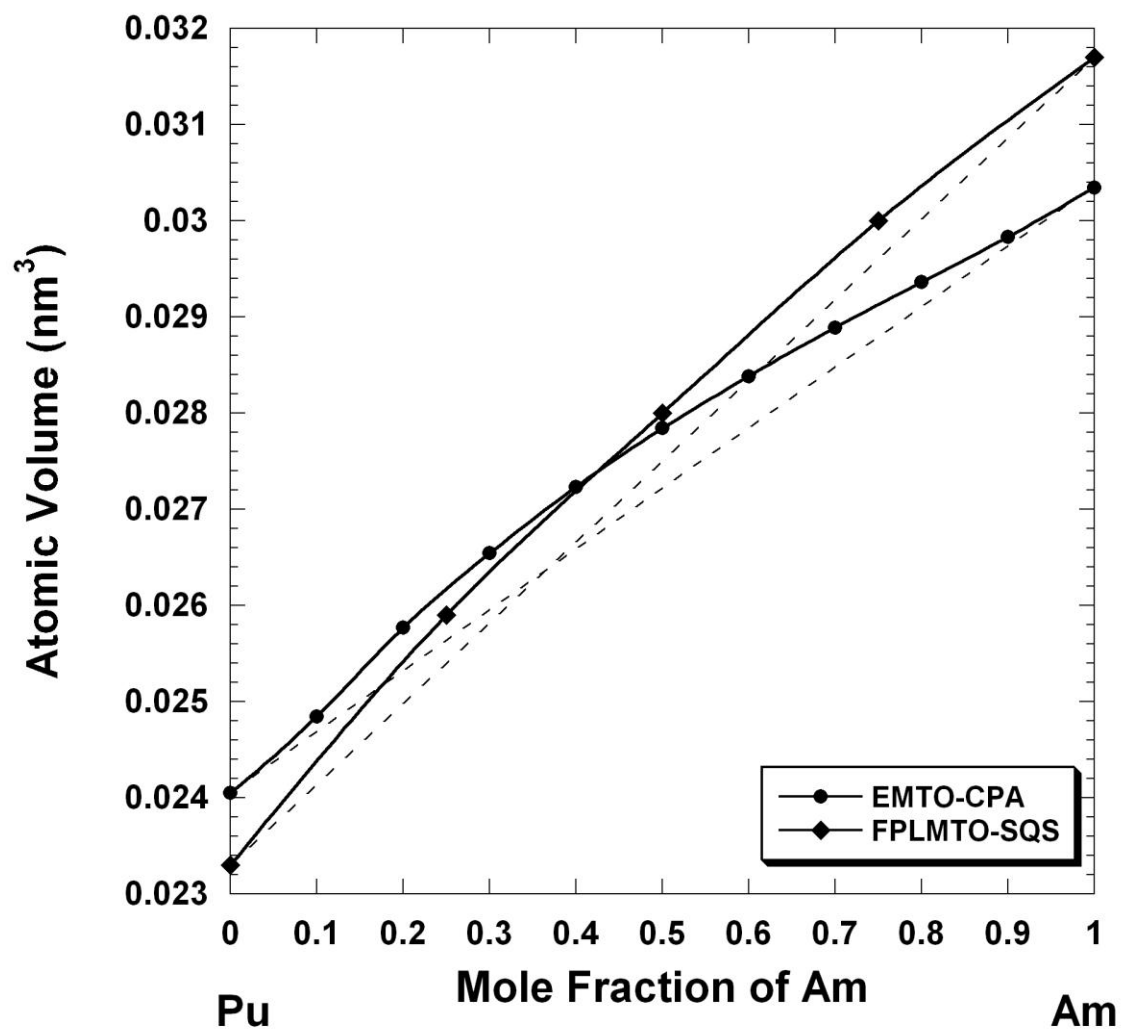


Figure 6.